# ALMA Survey of Orion Planck Galactic Cold Clumps (ALMASOP): Evidence for a Molecular Jet Launched at an Unprecedented Early Phase of Protostellar Evolution

Somnath Dutta[1] , Chin-Fei Lee[1] , Naomi Hirano[1] , Tie Liu[2,3] , Doug Johnstone[4,5] , Sheng-Yuan Liu[1] ,
Ken'ichi Tatematsu[6,7] , Paul F. Goldsmith[8] , Dipen Sahu[1] , Neal J. Evans[9] , Patricio Sanhueza[7,10] , Woojin Kwon[11,12] ,
Sheng-Li Qin[13] , Manash Ranjan Samal[14] , Qizhou Zhang[15] , Kee-Tae Kim[16,17] , Hsien Shang[1] , Chang Won Lee[16,17] ,
Anthony Moraghan[1] , Kai-Syun Jhan[1] , Shanghuo Li[16] , Jeong-Eun Lee[18] , Alessio Traficante[19] , Mika Juvela[20] ,
Leonardo Bronfman[21] , David Eden[22] , Archana Soam[23] , Jinhua He[21,24,25] , Hong-li Liu[13] , Yi-Jehng Kuan[26] ,
Veli-Matti Pelkonen[27] , Qiuyi Luo[2], Hee-Weon Yi[16] , and Shih-Ying Hsu[1,28]

[1] Institute of Astronomy and Astrophysics, Academia Sinica, Roosevelt Road, Taipei 10617, Taiwan, R.O.C.; sdutta@asiaa.sinica.edu.tw, cflee@asiaa.sinica.edu.tw
[2] Shanghai Astronomical Observatory, Chinese Academy of Sciences, 80 Nandan Road, Shanghai 200030, People's Republic of China
[3] Key Laboratory for Research in Galaxies and Cosmology, Chinese Academy of Sciences, 80 Nandan Road, Shanghai 200030 People's Republic of China
[4] NRC Herzberg Astronomy and Astrophysics, 5071 West Saanich Road, Victoria, BC V9E 2E7, Canada
[5] Department of Physics and Astronomy, University of Victoria, Victoria, BC V8P 1A1, Canada
[6] Nobeyama Radio Observatory, National Astronomical Observatory of Japan, National Institutes of Natural Sciences, 462-2 Nobeyama, Minamimaki, Minamisaku, Nagano 384-1305, Japan
[7] Department of Astronomical Science, SOKENDAI (The Graduate University for Advanced Studies), 2-21-1 Osawa, Mitaka, Tokyo 181-8588, Japan
[8] Jet Propulsion Laboratory, California Institute of Technology, 4800 Oak Grove Drive, Pasadena, CA 91109, USA
[9] Department of Astronomy, The University of Texas at Austin, 2515 Speedway, Stop C1400, Austin, TX 78712-1205, USA
[10] National Astronomical Observatory of Japan, National Institutes of Natural Sciences, 2-21-1 Osawa, Mitaka, Tokyo 181-8588, Japan
[11] Department of Earth Science Education, Seoul National University, 1 Gwanak-ro, Gwanak-gu, Seoul 08826, Republic of Korea
[12] SNU Astronomy Research Center, Seoul National University, 1 Gwanak-ro, Gwanak-gu, Seoul 08826, Republic of Korea
[13] Department of Astronomy, Yunnan University, and Key Laboratory of Particle Astrophysics of Yunnan Province, Kunming, 650091, People's Republic of China
[14] Physical Research Laboratory, Navrangpura, Ahmedabad, Gujarat 380009, India
[15] Center for Astrophysics—Harvard & Smithsonian, 60 Garden Street, Cambridge, MA 02138, USA
[16] Korea Astronomy and Space Science Institute (KASI), 776 Daedeokdae-ro, Yuseong-gu, Daejeon 34055, Republic of Korea
[17] University of Science and Technology, Korea (UST), 217 Gajeong-ro, Yuseong-gu, Daejeon 34113, Republic of Korea
[18] School of Space Research, Kyung Hee University, Yongin-Si, Gyeonggi-Do 17104, Republic of Korea
[19] IAPS-INAF, via Fosso del Cavaliere 100, I-00133, Rome, Italy
[20] Department of Physics, P.O.Box 64, FI-00014, University of Helsinki, Finland
[21] Departamento de Astronomía, Universidad de Chile, Casilla 36-D, Santiago, Chile
[22] Armagh Observatory and Planetarium, College Hill, Armagh, BT61 9DB, UK
[23] SOFIA Science Center, Universities Space Research Association, NASA Ames Research Center, Moffett Field, CA 94035, USA
[24] Yunnan Observatories, Chinese Academy of Sciences, 396 Yangfangwang, Guandu District, Kunming, 650216, People's Republic of China
[25] Chinese Academy of Sciences, South America Center for Astronomy, National Astronomical Observatories, CAS, Beijing 100101, People's Republic of China
[26] Department of Earth Sciences, National Taiwan Normal University, Taipei, Taiwan, R.O.C. & Institute of Astronomy and Astrophysics, Academia Sinica, Roosevelt Road, Taipei 10617, Taiwan, R.O.C.
[27] Institut de Ciències del Cosmos, Universitat de Barcelona, IEEC-UB, Martí i Franquès 1, E-08028 Barcelona, Spain
[28] National Taiwan University (NTU), No. 1, Section 4, Roosevelt Road, Taipei 10617, Taiwan, R.O.C.
Received 2022 January 16; revised 2022 April 12; accepted 2022 April 13; published 2022 June 2

## Abstract

Protostellar outflows and jets play a vital role in star formation as they carry away excess angular momentum from the inner disk surface, allowing the material to be transferred toward the central protostar. Theoretically, low-velocity and poorly collimated outflows appear from the beginning of the collapse at the first hydrostatic core (FHSC) stage. With growing protostellar core mass, high-density jets are launched, entraining an outflow from the infalling envelope. Until now, molecular jets have been observed at high velocity ($\gtrsim 100\,\mathrm{km\,s^{-1}}$) in early Class 0 protostars. We, for the first time, detect a dense molecular jet in SiO emission with low velocity ($\sim 4.2\,\mathrm{km\,s^{-1}}$, deprojected $\sim 24\,\mathrm{km\,s^{-1}}$) from source G208.89–20.04Walma (hereafter G208Walma) using ALMA Band 6 observations. This object has some characteristics of FHSCs, such as a small outflow/jet velocity, extended 1.3 mm continuum emission, and $N_2D^+$ line emission. Additional characteristics, however, are typical of early protostars: collimated outflow and SiO jet. The full extent of the outflow corresponds to a dynamical timescale of $\sim 930^{+200}_{-100}$ yr. The spectral energy distribution also suggests a very young source having an upper limit of $T_{\mathrm{bol}} \sim 31$ K and $L_{\mathrm{bol}} \sim 0.8\,L_\odot$. We conclude that G208Walma is likely in the transition phase from FHSC to protostar, and the molecular jet has been launched within a few hundred years of initial collapse. Therefore, G208Walma may be the earliest object discovered in the protostellar phase with a molecular jet.

*Unified Astronomy Thesaurus concepts:* Star formation (1569); Low mass stars (2050); Stellar jets (1607); Stellar winds (1636); Protostars (1302); Astrochemistry (75); Stellar mass loss (1613); Stellar evolution (1599); Young stellar objects (1834); Early stellar evolution (434)

## 1. Introduction

In the standard theory of low-mass star formation (Shu et al. 1987), a prestellar core contracts quasistatically into a dense core (e.g., Larson 1969; Nakano 1979; Lizano & Shu 1987),

and dynamical inside-out collapse follows the formation of a singular isothermal sphere (Shu 1977). In the presence of a magnetic field, an extended pseudo-disk (appearing as a flattened envelope) of a few thousand astronomical units forms perpendicular to the field threading the core (Galli & Shu 1993) during this transition phase from prestellar core to protostar formation (Li & Shu 1996; Allen et al. 2003). Very slow and poorly collimated outflows, with velocity $<10\,\mathrm{km\,s}^{-1}$, can emerge from cores having initial rotation (Allen et al. 2003; Hennebelle & Fromang 2008; Mellon & Li 2008). In some magnetohydrodynamic (MHD) simulations, a transient object called the first (opaque) core (later often dubbed the first hydrostatic core, FHSC) can appear at the center of the pseudo-disk (e.g., Tomisaka 2002; Ciardi & Hennebelle 2010). The candidate FHSC may have an observed spectral energy distribution (SED) intermediate between those of prestellar cores and Class 0 sources (Maureira et al. 2020).

Protostellar outflows and jets are among the most intriguing phenomena associated with the accretion process during star formation because they are believed to carry away excess angular momentum from the disk surface, therefore allowing material to fall onto the central protostar (Bally 2016; Lee 2020). Theoretically, an outflow of low-density extended material is expected to appear at the earliest phase of the collapse process, i.e., the first core formation stage (Larson 1969; Machida 2014). In contrast, high-density jets are expected to be launched a few hundred years after the initial collapse, possibly from the second core (protostar). With time, the fast jet will catch up with the tips of the previous slow outflow (Tomisaka 2002; Machida 2014; Machida & Basu 2019). To date, molecular jets with very high jet velocities, $>100\,\mathrm{km\,s}^{-1}$, and mass-loss rates, $\gtrsim 10^{-6}\,M_{\odot}\,\mathrm{yr}^{-1}$, have been observed around Class 0 protostars (Lee 2020). While FHSC candidates and their associated outflows have been reported (e.g., Chen et al. 2012; Maureira et al. 2020), the start of the fast jet-launching phase during the protostellar collapse, i.e., the intermediate stage between the FHSC and protostar formation, remains less explored observationally.

A sample of extremely cold dense cores has been observed as part of the ALMA Survey of Orion Planck Galactic Cold Clumps (ALMASOP; Dutta et al. 2020), which opens the opportunity to detect the earliest stage of protostars and investigate the initial condition of protostellar evolution. In this manuscript, we present the detection of a dense molecular SiO jet at an unprecedentedly early protostellar stage, possibly the FHSC-to-protostellar transition phase, in the dense core G208.89−20.04Walma (hereafter G208Walma), located at a distance of ∼400 pc (the average distance of Orion star-forming regions; Kounkel et al. 2018). This is potentially the first detection of a SiO jet at such an early evolutionary stage. In Section 2, we describe the observations used. Section 3 deals with the outflow, jet, and envelope properties. The evolutionary phase of G208Walma is discussed in Section 4, with the conclusion in Section 5.

## 2. Observations

G208Walma was observed with ALMA as part of the ALMASOP survey of extremely young dense cores (Project ID:2018.1.00302.S; PI: Tie Liu) in Band 6 (see Dutta et al. 2020 for more details on ALMASOP). This paper discusses 1.3 mm dust continuum, $C^{18}O(2-1)$, $N_2D^+(3-2)$, $CO(2-1)$, $SiO(5-4)$, and three $H_2CO$ transitions: $3(0,3)-2(0,2)$, $3(2,2)$−

$2(2,1)$, and $3(2,1)-2(2,0)$. The calibration of the acquired visibilities was performed with the standard pipeline in CASA 5.4 (McMullin et al. 2007). Two sets of continuum and line cubes were generated with the TCLEAN task: (i) combining visibilities of three configurations (i.e., TM1+TM2+ACA), which produces an image of a typical synthesized beam size $\sim 0.\!''41 \times 0.\!''34$ ($-69°$), and (ii) only using the 7 m ACA configuration to produce a typical synthesized beam size $\sim 7.\!''92 \times 4.\!''42$ ($-80°$) for the continuum and $\sim 8.\!''42 \times 4.\!''67$ ($-79°$) for the line cubes. From here on, we refer to the first case as high resolution and the latter case as low resolution. We applied a robust weighting factor of $R_w = +2.0$ (natural weighting) for the 1.3 mm ACA continuum, which is adequate to achieve maximum continuum flux for dust mass estimation. For the remaining cases, we utilized $R_w = +0.5$. The continuum maps were generated with a threshold of $3\sigma$, where $\sigma$ is the theoretical sensitivity. The line cubes have a velocity resolution of $\sim 1.4\,\mathrm{km\,s}^{-1}$ and typical sensitivity of $\sim 3\,\mathrm{mJy\,beam}^{-1}$ at high resolution and $30\,\mathrm{mJy\,beam}^{-1}$ at low resolution. More details on the data analyses are presented by Dutta et al. (2020).

## 3. Results

### 3.1. Physical Structure of the CO Outflow

The $^{12}$CO emission map integrated over velocity range 2.8–8.4 km s$^{-1}$ and the position–velocity (PV) diagram along the outflow/jet axis are shown in Figures 1(a) and b, respectively. SiO contours are overplotted in red in Figure 1(b). CO and SiO emissions are extended in the northeast direction with a position angle of ∼80°. The velocity axis in Figure 1(b) is the velocity offset from the systemic velocity, $V_{sys} = 7\,\mathrm{km\,s}^{-1}$, estimated from the $N_2D^+$ emission. Here velocity offset, $V_{off} = |V_{obs}-V_{sys}|$, where $V_{obs}$ is the observed channel velocity. Visual inspection of the channel maps (Figure A1) and CO/SiO spectra (Figure A2) suggests that emission beyond 4.2 km s$^{-1}$ velocity offset is tracing ambient material. In Figure 1(b), the emission in the northern lobe (positive position offset) has two clear isolated parallel components: one around the source velocity and another beyond 4.2 km s$^{-1}$ velocity offset, which is likely the ambient material. Similarly, the southern lobe (negative position offset) is combined with ambient cloud at >4.2 km s$^{-1}$ velocity offset. In Figure 1(b), the shaded region in blue at the end of each lobe, beyond 10″, is dominated by ambient material in the combined configuration TM1+TM2+ACA maps. Based on SiO and CO emission, the maximum observed velocity offset ($V_{obs,out}$) of the outflow/jet is 4.2 km s$^{-1}$. The PV diagrams and the spectra of CO and SiO do not exhibit any high-velocity component, therefore, it is difficult to disentangle the velocity distribution of the outflow, swept-up material, and jet components.

Following the simple analytical model by Lee et al. (2000), the physical structure of the outflow shell in CO emission is described by the equation $z = CR^2$, where $R$ is the (cylindrical) radial distance from the outflow axis $z$ and $C$ is a proportionality constant. In Figure 1(a), fitting a parabola to the outermost contour of the outflow yields $C = 3.3$ arcsec$^{-1}$ and 5.0 arcsec$^{-1}$ for the southern and northern lobes, respectively. With these $C$ values, we aim to fit parabolas to the respective outflow lobes in the PV diagram (Figure 1(b)). We are unable to obtain a fit to the PV structures. We display
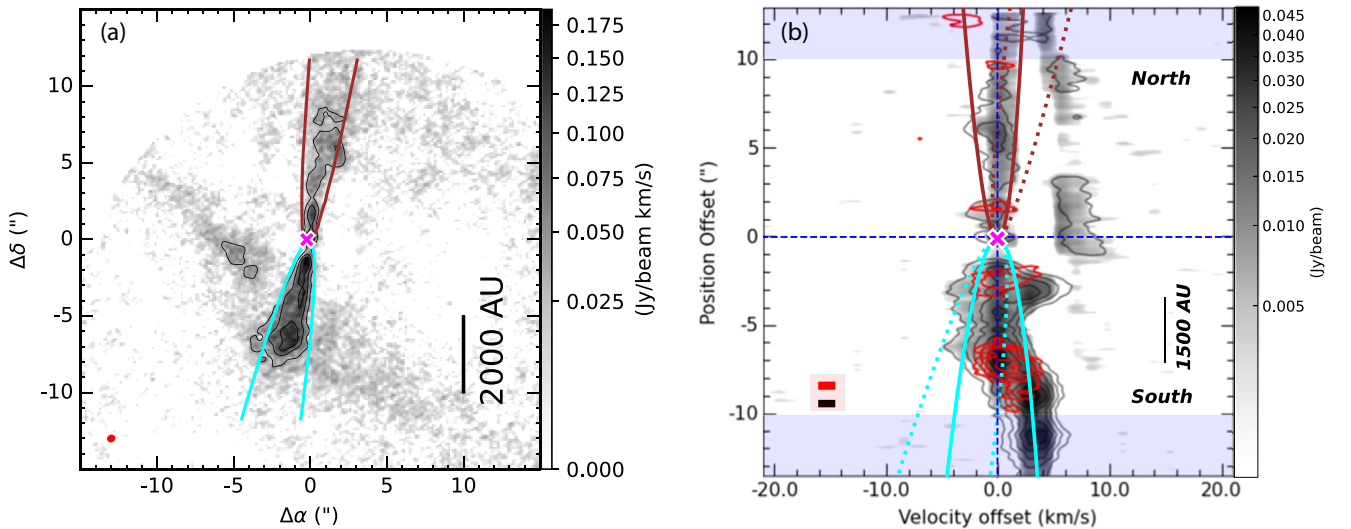
**Figure 1.** (a) High-resolution ALMA map of G208Walma in CO emission integrated over 2.8–8.4 km s$^{-1}$. The contours are overplotted at $3 \times (1, 2, 3, 6, 9)\sigma$, where sensitivity $\sigma = 12$ mJy beam$^{-1}$ km s$^{-1}$. The synthesized beam size $\sim 0\farcs41 \times 0\farcs34$ is shown in the lower left. CO emission is extended in the northeast direction with a position angle of $\sim 80°$. The cyan and red parabolas are best fits for the proportionality constant $C = 3.3$ arcsec$^{-1}$ and 5.0 arcsec$^{-1}$, respectively (see Section 3.1 for details). (b) PV diagram along the jet axis of the $^{12}$CO(2−1) emission. The black contours are at $3 \times (1, 2, 3, 4, 5, 6)\sigma$, where $\sigma = 1.0$ mJy beam$^{-1}$. The SiO contours are overplotted in red at $(2.5, 3.5, 4.5, 6.5, 7.5, 18)\sigma$, where $\sigma = 0.9$ mJy beam$^{-1}$. The beam sizes are shown in the lower left for CO (in black) and SiO (in red) emission. The solid and dotted parabolas are for $i_a \sim 1°$ and $10°$, respectively. Cyan and red represent the southern and northern lobes, respectively. The blue dashed straight lines, representing the zero axis, cross at the source position (magenta cross). The emission within the blue-shaded region at $>10''$ is possibly tracing ambient material (see text for details). Linear scale bars are shown in both panels.

two example fits assuming inclination angles $i_a = 1°$ and $10°$ for both lobes. From the ratio of the major to minor axes in 1.3 mm continuum and $N_2D^+$ emission (see Section 3.4), we estimated an $i_a \sim 20°$. However, geometrically thick emission from young stars might not demonstrate the actual orientation of the disk. Thus, we conclude that the $i_a$ could be in the range $1°$–$20°$. We therefore assume an intermediate $i_a \sim 10°$ for G208Walma, which is utilized for deprojection of other observed parameters.

### 3.2. Detection of a Dense Molecular Jet

Figures 2(a)–(d) show the high-resolution integrated intensity maps in SiO (5–4) and three H$_2$CO transitions. A rotation diagram using the energy levels of the H$_2$CO transitions is shown in Figure 3. High-resolution integrated intensity CO contours from Figure 1(a) are overplotted in Figures 2(a)–(d) for comparison, and the low-resolution CO contours are displayed in Figure 4(c).

In Section 3.1, we found that the maximum flow velocity in CO emission is $V_{max,CO} \sim 4.2$ km s$^{-1}$ (Table 1), and similarly in SiO, $V_{max,SiO} \sim 4.2$ km s$^{-1}$. Both SiO and CO emission exhibit low-velocity components with a very similar velocity range, complicating the separation of the jet component from swept-up material (outflow) based on flow velocity only. Therefore, we define the jet component by considering the density perspective using SiO and CO. CO emission above the $3\sigma$ contour is considered to be the outflow shell, as shown in Figure 1(a). On the other hand, observations of other sources in SiO (5–4) have shown that it traces the dense shocked gas, and SiO (5–4) emission along the outflow axis mainly implies the high-density jet (e.g., Bally 2016; Lee 2020 and references therein). We compute the critical density for SiO (5–4) emission as $\sim 2.5$–$3.0 \times 10^6$ cm$^{-3}$ for jet temperatures between 50 and 300 K, where the Einstein $A$ coefficient is adopted from the CDMS database (Müller et al. 2001) and collisional rate coefficients from Balança et al. (2018). Such critical densities should be reached

only in the jet or knots. Therefore, despite the low velocity of the outflow/jet material, we consider the SiO (5–4) emission, found along the outflow/jet axis of G208Walma, to indicate the jet component.

A few knot-like structures (B1, B2, and R1 in Figure 2) are prominent in SiO emission and are also traced by CO and higher transitions of H$_2$CO emission (Figures 2(c)–(d)). Two knots closest to the source (B1 and R1 in Figure 2(a)) on the southern and northern lobes are possibly part of the jet, whereas the SiO emission at the outermost part of the southern lobe (B2 in Figure 2(a)) might be part of the collision zone between the jet/outflow and ambient material (see also Figures 1(b), 4(d), and A1). The maximum outflow and jet observed velocity, $V_{obs,out} = 4.2$ km s$^{-1}$, based on CO and SiO emission, corresponds to a deprojected jet velocity of $V_j \sim 24$ km s$^{-1}$ for an assumed inclination angle, $i_a = 10°$ (see Section 3.1 for details). These outflow/jet properties are listed in Table 1.

The jet mass-loss rate $\dot{M_j}$ was derived using the average CO emission from the two knot areas close to the source (B1 and R1 in Figure 2). Assuming optically thin emission in the jet, we estimate a beam-average CO column density ($N_{CO}$) of $\sim 2.16 \times 10^{16}$ cm$^{-2}$. We assume a high CO excitation temperature of $T_{ex,jet} \sim 150$ K, because the jet emission is associated with internal shocks at high temperature (Gibb et al. 2004; Lee et al. 2007, 2010). $N_{CO}$ is then converted into beam-averaged H$_2$ column density, $N_{H_2}$, assuming a CO abundance ratio, $X_{CO} = N_{CO}/N_{H_2} = 4 \times 10^{-4}$ (Glassgold et al. 1991). However, we note that this ratio could be as small as $\sim 10^{-4}$ (Hirano et al. 2010; Yıldız et al. 2015), hence the measured $N_{H_2}$ should be considered a lower limit. Using Equation (A1) from Appendix A.2, the total jet mass-loss rate ($\dot{M_j}$) is estimated to be $\sim 1.96 \times 10^{-7} M_\odot$ yr$^{-1}$, considering the deprojected velocity. A very small mechanical luminosity ($L_{mech} \sim 1.78 \times 10^{-3} L_\odot$) is found. Similar values of $\dot{M_j}$ and $L_{mech}$ were also observed toward other Class 0 and Class I protostars with SiO jets (e.g., Podio et al. 2021; Dutta et al. 2022).
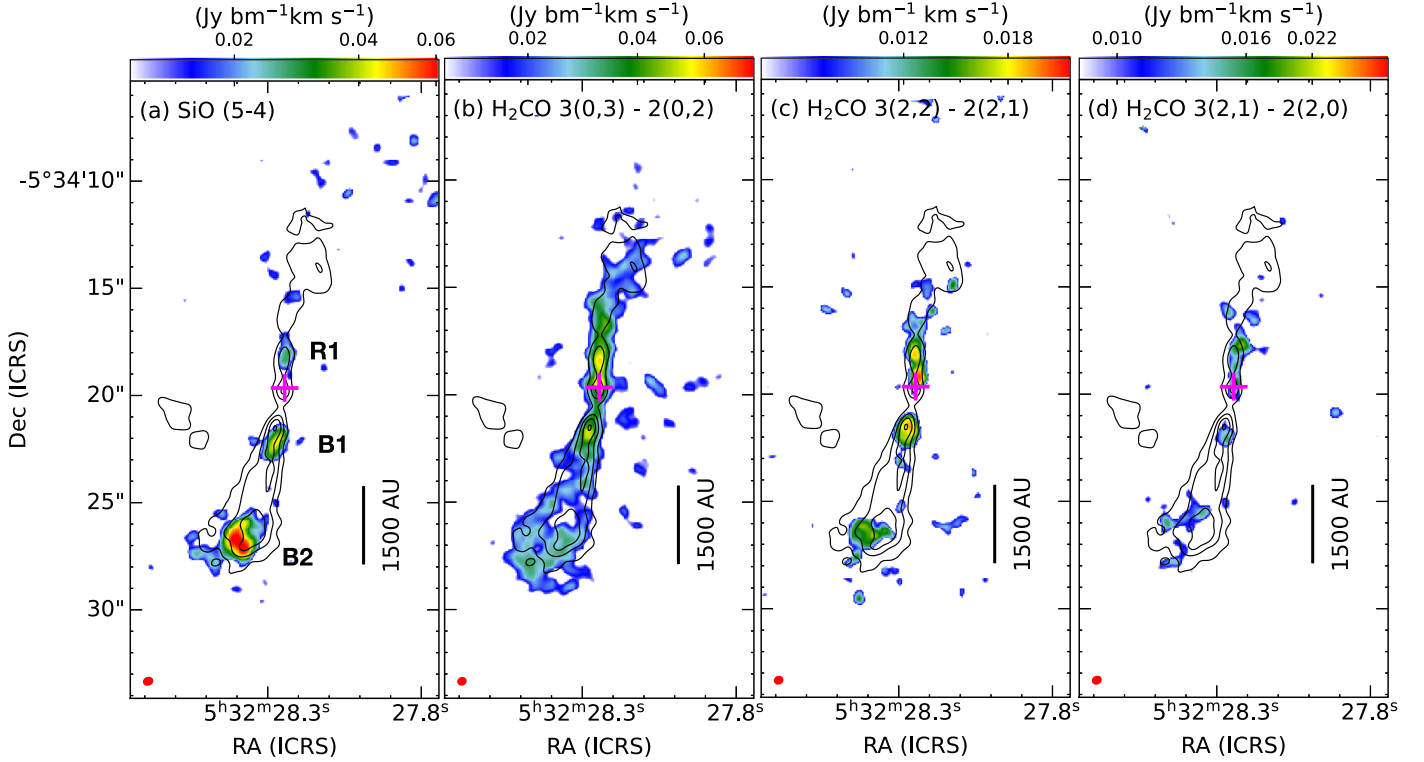
**Figure 2.** High-resolution ALMA integrated maps (moment 0) of G208Walma in (a) SiO J = 5−4 integrated over velocity 2.8–8.4 km s$^{-1}$ with a sensitivity of ~10 mJy beam$^{-1}$ km s$^{-1}$, (b) H$_2$CO 3(0, 3)−2(0, 2) with a sensitivity of ~9.4 mJy beam$^{-1}$ km s$^{-1}$ (c) H$_2$CO 3(2, 2)−2(2, 1) with a sensitivity of ~6.5 mJy beam$^{-1}$ km s$^{-1}$, and (d) H$_2$CO 3(2, 1)−2(2, 0) with a sensitivity of ~6 mJy beam$^{-1}$ km s$^{-1}$ at a spatial resolution of 140 au. All H$_2$CO transitions are integrated over velocities 7.0–8.4 km s$^{-1}$. $^{12}$CO(2–1) contours have the same meaning as Figure 1(a). The prominent knot-like structures are marked as B1, B2 in the southern lobe, and R1 in the northern lobe. The continuum peak position is marked with a magenta cross in all panels. The beam sizes are shown in red on the lower left (typically ~0″41 × 0″34). The linear scale bars are shown in all the panels.
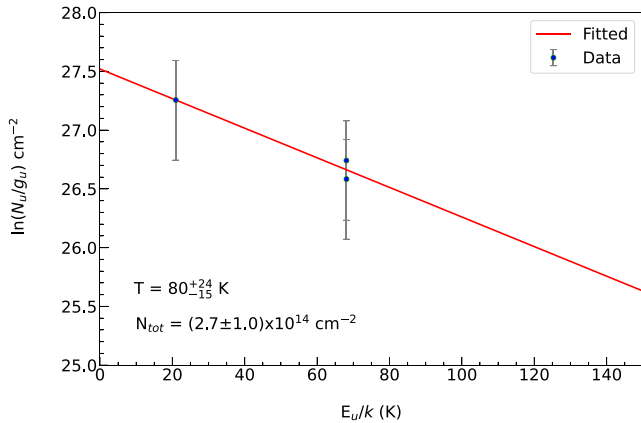


**Figure 3.** Rotation diagram for molecular transitions of H$_2$CO. The diagram is derived from the line intensities in the outflow/jet of Figures 2(b)–(d), as listed in Table 2. The error bars indicate the uncertainty in our measurements, which are assumed to be 40% of the estimated data values. The solid line is a linear fit to the data. The rotational temperature and column density are estimated as ~80$^{+24}_{-15}$ K and (2.7 ± 1.00) × 10$^{14}$ cm$^{-2}$ from the fitting.

For the low-density outflow, we assume a smaller mean specific excitation temperature of $T_{ex,out} = 50$ K with a smaller abundance ratio, $X_{CO} \sim 10^{-4}$, than that for the jet (Yıldız et al. 2015; Dutta et al. 2022). We use a lower temperature here because the low-density outflow is coasting into the ambient material of the cooler environment. Using Equation (A3) from Appendix A.3, we estimate a total outflow force ($F_{CO}$) of ~0.8 × 10$^{-8}$ $M_\odot$ km s$^{-1}$ yr$^{-1}$ for the entire CO emission. We note that $F_{CO}$ for each channel is proportional to the velocity of

that channel, $V_k$. G208Walma has velocity dispersion on both sides of the systemic velocity ($V_{sys} = 7.0$ km $^{-1}$), which makes it difficult to estimate the exact $V_k$ from our low-velocity resolution (~1.4 km s$^{-1}$) observations. High-velocity-resolution observations, therefore, might alter the outflow force measurement by a factor of 2–4. Furthermore, for G208Walma, the outflow emission is collimated and mostly covers the emitting area of the jet, where $T_{ex,out}$ is likely higher. Therefore, the estimated $F_{CO}$ should be a lower limit.

Low-resolution ACA maps offer a maximum field of view, covering the full extent of the outflow lobes (Figure 4(c)). From this map, we estimate an average length for the lobes of ~12″ (~4800 au), which corresponds to an average deprojected dynamical timescale of $t_{dyn} \sim 930^{+200}_{-100}$ yr (Table 1) for $i_a = 10°$. Here, the error bars are derived based on the uncertainty in the before-projection lobe length estimation. A change of $i_a \sim 5°$ can alter this value by ~50%.

Similar to the CO analysis, we estimate a mean SiO column density ($N_{SiO}$) of 4.5 × 10$^{13}$ cm$^{-2}$ from the mean integrated SiO emission with the assumption of optically thin emission and a $T_{ex,jet}$ of 150 K within the jet. The average SiO/CO abundance ratio, $X$[SiO/CO] is ~5.0 × 10$^{-4}$. Such high SiO abundance has been previously observed during the very early stage of the protostellar collapse (Hirano et al. 2010; Tabone et al. 2020; Podio et al. 2021; Dutta et al. 2022).

### 3.3. H$_2$CO along the Jet Axis

H$_2$CO commonly traces both outflow and disk/envelope emission. If carbon molecules dissociate due to high
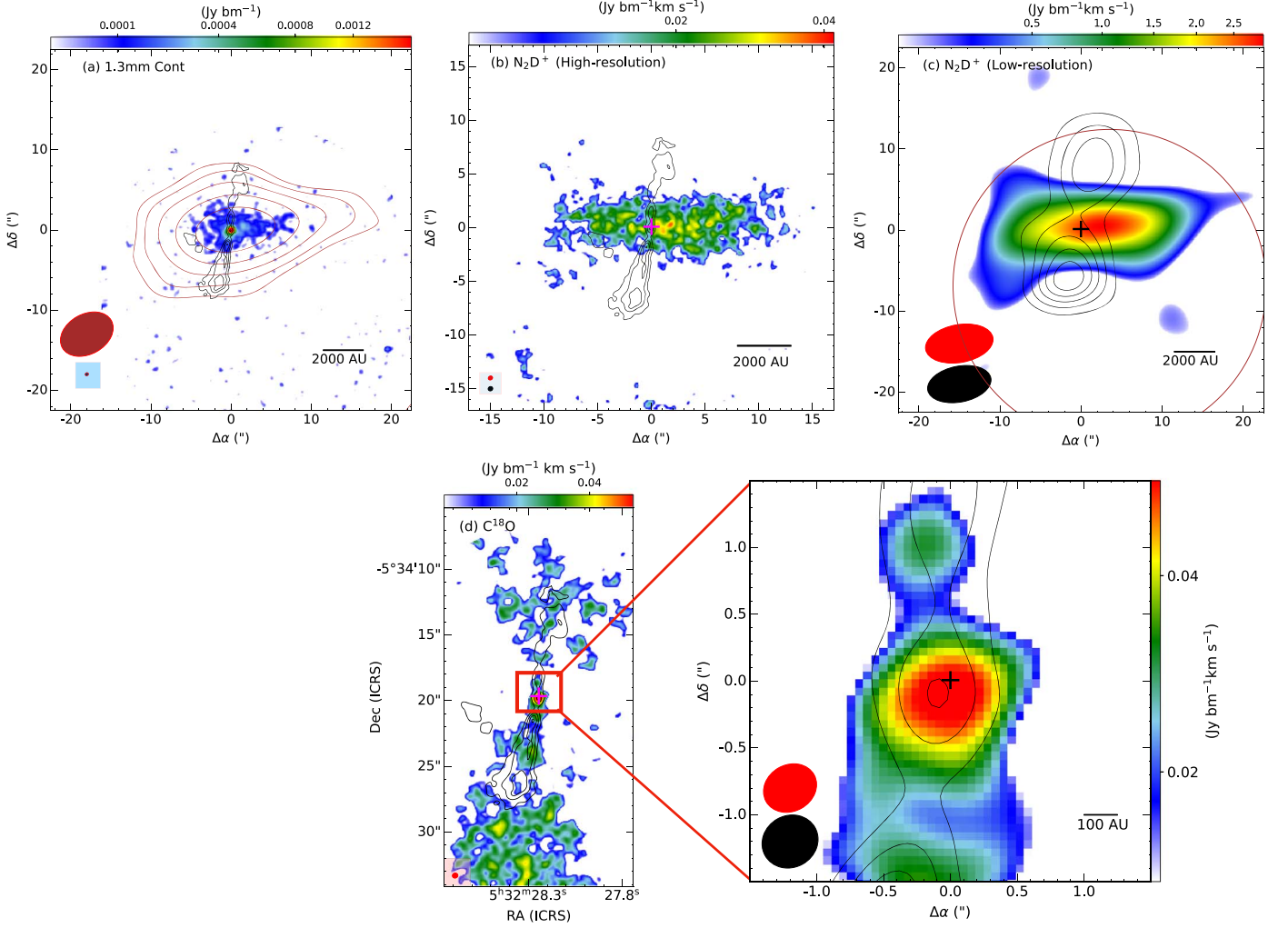
**Figure 4.** (a) High-resolution ALMA 1.3 mm continuum map with a sensitivity of 0.035 mJy beam$^{-1}$ (beam size in red in the lower left). Low-resolution 7 m ACA contours are overplotted in brown at $3 \times 2^n \sigma$, where $n = 1, 2, 3, 4, 5$, and 6 and sensitivity $\sigma = 0.4$ mJy beam$^{-1}$ (beam size in brown in the lower left). (b) High-resolution $N_2D^+$ map integrated over velocities 5.6–7.0 km s$^{-1}$ with a sensitivity of 10 mJy beam$^{-1}$ km s$^{-1}$. (c) Low-resolution $N_2D^+$ map integrated over velocities 5.6–7.0 km s$^{-1}$ with a sensitivity of 0.17 Jy beam$^{-1}$ km s$^{-1}$. The CO contours of 7 m ACA observations are overplotted at $3 \times (1, 2, 3, 4, 5, 6)\sigma$, where $\sigma = 0.2$ Jy beam$^{-1}$ km s$^{-1}$. The cross indicates the 1.3 mm continuum peak. The large circle indicates the combined TM1+TM2+ACA primary beam. (d) High-resolution $C^{18}O$ map integrated over velocities 7.0–8.4 km s$^{-1}$ with a sensitivity of 10 mJy beam$^{-1}$ km s$^{-1}$. The central part is also shown in zoomed view. The CO contours have the same meaning as in Figure 1(a). Beam sizes of CO (black) and $C^{18}O$ emission map (red) are also shown in the lower left in each panel. The linear scale bars are shown in all the panels.

temperatures ($>20$ K), $H_2CO$ molecules synthesize around protostars (Öberg et al. 2017). Figures 2(b)–(d) display three transitions of $H_2CO$. From the maps, it is not clear whether $H_2CO$ traces either the disk or envelope for this source, although it efficiently traces the outflow lobes. The lower transitions are excited at low temperatures, which can trace the entire outflow lobe (e.g., Figure 2(b)). The higher transitions are more concentrated toward the dense knot structures along with the jet (e.g., Figure 2(d)).

The average observed integrated flux at the knot positions for the three transitions of $H_2CO$ is listed in Table 2. The Einstein coefficients ($A_{ul}$) and upper energy levels ($E_u$) are obtained from Spatalogue (https://splatalogue.online//). We derive the mean excitation temperature and column density in the outflow/jet using the $^{12}CO$ rotational temperature diagram. Here we assume optically thin emission and the same excitation temperature for all transitions. Figure 3 displays the column density per statistical weight ($N_u^{thin}/g_u$) as a function of the upper energy level ($E_u$) of the lines (see Table 2 for

parameters). Here $N_u^{thin} = (8\pi k\nu^2/hc^3 A_{ul})I$, where the integrated line intensity is $I = \int T_B dv$ for brightness temperature $T_B$. The best-fit rotational temperature is derived as $T_{rot} = 80^{+24}_{-15}$ K. Assuming this temperature represents the excitation temperature of the jet/outflow, we estimated a total column density $N_{H_2CO}^{tot} \sim (2.7 \pm 1.0) \times 10^{14}$ cm$^{-2}$. Note that the $H_2CO$ transitions may trace different components in different transitions, such as the outflow in the lower transitions and the jet in the higher transitions. Thus, the computed $T_{rot}$ may represent an intermediate temperature between the jet and outflow and is therefore not used in Section 3.2 as either outflow or jet excitation temperature.

### 3.4. Envelope Emission

Figure 4(a) shows the 1.3 mm dust continuum emission. At high resolution, the continuum emission is resolved out, whereas at low resolution (ACA), the emission is quite extended, revealing the source envelope. The observed line

**Table 1**
Physical Properties of the Jet and Outflow

| Parameter (Units) | South | North | Total |
|---|---|---|---|
| Jet | | | |
| $V_{\mathrm{obs,out}}$[a] (km s$^{-1}$) | 4.2 | 4.2 | ⋯ |
| $N_{\mathrm{CO}}$ ($10^{16}$ cm$^{-2}$) | 2.30 | 2.02 | ⋯ |
| $\dot{M}_{\mathrm{j}}$ ($10^{-7}\,M_\odot$ yr$^{-1}$) | 1.01 | 0.95 | 1.96 |
| $L_{\mathrm{mech}}$ ($10^{-3}\,L_\odot$) | 1.03 | 0.75 | 1.78 |
| $N_{\mathrm{SiO}}$ ($10^{13}$ cm$^{-2}$) | 2.7 | 1.8 | ⋯ |
| X[SiO/CO] ($10^{-4}$) | 5.8 | 4.2 | ⋯ |
| Outflow | | | |
| Size[b] ($10^{3}$ au) | 4.5 | 5.0 | ⋯ |
| $t_{\mathrm{dyn}}$[b] (yr) | 890 | 970 | ⋯ |
| $\dot{F}_{\mathrm{CO}}$ ($10^{-8}\,M_\odot$ km s$^{-1}$ yr$^{-1}$) | 0.5 | 0.3 | 0.8 |

**Notes.**
[a] The outflow/jet velocity ($V_{\mathrm{obs,out}}$) is estimated to be 4.2 km s$^{-1}$. The deprojected jet velocity, $V_j = 24$ km s$^{-1}$, was obtained for an inclination angle of 10°.
[b] Estimated based on the full outflow extension as observed at the 7 m ACA primary beam.

emission associated with the outflow is mostly confined within the envelope. Gaussian fitting to the low-resolution ACA image provides a flux density ($F_\nu$) of 69.0 mJy, with a peak emission of 34.5 mJy beam$^{-1}$. The Gaussian fitted deconvolved parameters are tabulated in Table 3. The core has an effective radius of $R_{\mathrm{eff}} = \sqrt{\mathrm{Maj} * \mathrm{Min}} \sim 2500$ au.

We derive the dust mass corresponding to this $F_\nu$ under the assumption of optically thin emission, using the equation

$$M_{\mathrm{Env}} \sim \frac{D^2 F_\nu}{B_\nu(T_{\mathrm{dust}})\kappa_\nu}, \qquad (1)$$

where $D$ is the distance to the Orion molecular cloud $\sim$400 pc (Kounkel et al. 2018) and $B_\nu$ stands for the Planck blackbody function at a dust temperature of $T_{\mathrm{dust}}$. Fitting the Planck blackbody function to the multiwavelength fluxes provided in Appendix B, we estimate $T_{\mathrm{dust}}$ of $15 \pm 5$ K. $\kappa_\nu$ represents the mass opacity of the protostellar core at 1.3 mm, which can be expressed as $\kappa_\nu = 0.00899(\nu/231\ \mathrm{GHz})^\beta$ cm$^2$ g$^{-1}$ (Lee et al. 2018) in the early phase for coagulated dust particles with no ice mantles (see also OH5: column 5 of Ossenkopf & Henning 1994) given a gas-to-dust mass ratio of 100 and spectral index $\beta \sim 1.7$ for the envelope. The final mass is estimated to be $M_{\mathrm{Env}} \sim 0.38 \pm 0.14\,M_\odot$.

Deuterated species mainly trace the prestellar stage or very early phase of protostar evolution. Figures 4(b) and (c) delineate $N_2D^+$ emission at high and low resolution, respectively. Only two channels, at velocity 5.6–7.0 km s$^{-1}$, display $N_2D^+$ emission. The channel at 7.0 km s$^{-1}$ has the strongest emission and is considered the $V_{\mathrm{sys}}$ for G208Walma. G208Walma exhibits very extended $N_2D^+$ emission, which is quite similar in morphology to the 1.3 mm continuum emission. Interestingly, the $N_2D^+$ peak is $\sim$500 ± 300 au apart from the dust continuum peak, estimated from Gaussian fitting to both images. Here, we assume the error bar to be of order twice the high-resolution beam size. This separation is evident in both the high-resolution as well as the low-resolution map. Assuming optically thin emission and an excitation temperature

of 10 K, we derive an average $N_2D^+$ column density $N_{N_2D^+}$ $\sim 1.2 \times 10^{12}$ cm$^{-2}$.

$C^{18}O$ emission, displayed in Figure 4(d), usually originates from the compact central part of the source. Only two channels, at velocities 7.0 and 8.4 km s$^{-1}$, show $C^{18}O$ emission. For this source, the $C^{18}O$ emission is likely tracing the object as well as the ambient material. Given such complicated morphology, the true object emission is difficult to disentangle from our low-velocity resolution observations. Considering the uncertainties in estimation, we suggest that the $C^{18}O$ emission in the central part (zoomed view of 4(c)) is possibly originating from a small central compact core where $N_2D^+$ is weak. This implies that the gas surrounding the central protostar is heated above the CO evaporation temperature ($\sim$20 K). Another interesting fact to note is that, comparing Figures 2(a) and 4(c), the southern lobe of the outflow tip is possibly interacting with ambient material. Thus, the SiO emission there may be due to collisional excitation.

## 4. Discussion

A small observed outflow velocity, $V_{\mathrm{obs,out}} \lesssim 10$ km s$^{-1}$, is one of the main characteristics of candidate FHSCs (Hirano & Liu 2014; Maureira et al. 2020). G208Walma exhibits $V_{\mathrm{obs,out}} \sim 4.2$ km s$^{-1}$, analogous to those of FHSCs. However, the deprojected $V_j \sim 24.0$ km s$^{-1}$ is higher than that of the FHSC limit. The outflow is spatially extended up to 4800 au when deprojected and has a $t_{\mathrm{dyn}} \sim 930^{+200}_{-100}$ yr, which suggests that the object could be at a very early phase. The outflow lobes appear to be collimated in the high-resolution maps (Figures 2(a)–(d)), similar to Class 0 protostars.

A correlation between $F_{\mathrm{CO}}$ and $L_{\mathrm{bol}}$ has been investigated in the literature to probe the evolutionary stages of protostars (e.g., Bontemps et al. 1996). Using multiwavelength observed flux, we estimate the bolometric luminosity ($L_{\mathrm{bol}}$) and bolometric temperature ($T_{\mathrm{bol}}$) for G208Walma (see Appendix B for details). In Figure 5(a), we compare G208Walma with normal young stellar objects (YSOs), very low-luminosity objects (VeLLOs), proto-brown dwarfs (proto-BDs), and candidate FHSCs from Palau et al. (2014, see their Table 4 and Figure 7, and references therein) and Hsieh et al. (2016, see their Figure 13). Here we note that proto-BDs are also in the VeLLOs category. When the protostar evolves from the initial collapse phase, the luminosity of the central core increases. The accretion/ejection activity is also expected to increase up to a certain phase, possibly up to the late Class 0 or early Class I; consequently, the $F_{\mathrm{CO}}$ should increase with protostellar evolution. Therefore, the YSOs in Figure 5(a) exhibit higher $L_{\mathrm{bol}}$ and higher $F_{\mathrm{CO}}$ compared with the youngest protostars and candidate FHSCs, VeLLOs, and proto-BDs.

G208Walma appears much younger than YSOs like HH 211 and shares a lower limit of $F_{\mathrm{CO}}$ and an upper limit for $L_{\mathrm{bol}}$ with the VeLLOs, proto-BDs, and FHSCs in Figure 5(a). It is likely more evolved than the candidate FHSC L1451-mm. G208Walma is embedded within a large reservoir (effective radius $\sim$16,500 au) with a mass of $\sim$4.78 $M_\odot$, estimated from the 850 $\mu$m emission obtained by the James Clerk Maxwell Telescope (JCMT; island #25 in Mairs et al. 2016). From the 1.3 mm continuum emission, it possesses a thick envelope of mass >0.38 $M_\odot$. If we assume one-third of the envelope would be accreted to the central protostar, then even with the mass observed with ALMA, a star of mass >0.12 $M_\odot$ will form. Thus, G208Walma may not form a proto-BDs but rather a very

**Table 2**
H$_2$CO Line Properties

| Transition | Frequency (GHz) | log($A_{ul}$) (s$^{-1}$) | $E_u$ (K) | W (Jy bm$^{-1}$ km s$^{-1}$) | Line |
|---|---|---|---|---|---|
| 3(0, 3)–2(0, 2) | 218.222192 | −3.55037 | 20.95640 | 0.084 | JPL |
| 3(2, 2)–2(2, 1) | 218.475632 | −3.80403 | 68.09370 | 0.028 | JPL |
| 3(2, 1)–2(2, 0) | 218.760066 | −3.80235 | 68.11081 | 0.024 | JPL |

**Table 3**
Deconvolved Parameters of the Gaussian Fit at the ACA Continuum

| Deconvolved Parameters | Value (Units) |
|---|---|
| Flux | 69.0 ± 3.5 (mJy) |
| Peak | 34.5 ± 1.3 (mJy bm$^{-1}$) |
| Maj | 8.77 ± 0.77 ($''$) |
| Min | 4.45 ± 0.34 ($''$) |
| PA | 94.45 ± 4.75 (deg) |
| Mass | 0.38 ± 0.14 ($M_\odot$) |
| $R_{eff}$ | 2500 (au) |

low-mass star, and it may have already passed the FHSC phase or be transiting from an FHSC to a protostar.

Detection of SiO in a jet signifies very high accretion/ejection activity within a protostar. The SiO jet is usually launched from the earliest Class 0 protostars having very high jet mass loss ($\dot{M}_j \gtrsim 10^{-6} M_\odot$ yr$^{-1}$) and very high $V_j$ (>100 km s$^{-1}$) e.g., B335 (Bjerkeli et al. 2019) and HH 211 (Lee et al. 2018). Dense SiO emission is detected within the outflow cavity of G208Walma, although it exhibits a smaller $V_j$ and $\dot{M}_j$ ($\sim 1.96 \times 10^{-7} M_\odot$ yr$^{-1}$; Table 1), indicating that a protostar may have already formed inside the core that has passed through the second collapse phase or is transitioning from an FHSC to a protostar. To form SiO in the jet, the SiO needs to be synthesized from larger dust grains either (i) at the shock region in the jet through grain sputtering or (ii) at the dust sublimation zone near the protostellar core. In the first case, the shock velocity ($V_s$) is predicted to be $10 < V_s < 40$ km s$^{-1}$ (Schilke et al. 1997). For G208Walma, the observed $V_s$ is $\sim 4$ km s$^{-1}$ in the northern lobe, whereas the southern part is blended with ambient material and difficult to measure (Figure 1(b)). The $V_s$ could be affected largely due to our low sensitivity and low velocity resolution. For the latter case, the Si could have been released from grain surfaces in the dust sublimation zone near the object and synthesized into SiO. The $L_{bol}$ of 0.80 $L_\odot$ suggests that the dust sublimation radius could be <0.1 au (Millan-Gabet et al. 2007). A comparison of the measured X[SiO/CO] and $\dot{M}_j$ from Table 1 with the astrochemical model of Tabone et al. (2020, their Figure 12) suggests that the jet may have been launched from the outermost region of the dust-free zone, where the dust-to-gas ratio ($Q$) is relatively higher (0.1–0.01).

Schnee et al. (2012) detected extended SiO (2–1) emission from another very young source, Per-Bolo 45, at a distance of 20$''$ south of the object and with velocities within 1 km s$^{-1}$ of the ambient velocity. They interpreted this detection as tentative evidence for a jet in Per-Bolo 45. However, Maureira et al. (2020) extensively studied this object and suggested that this SiO (2–1) emission is possibly not associated with Per-Bolo 45; rather, it is a collision zone between Per-Bolo 45 and the outflow tip of another source SVS 13 c. They also concluded that Per-Bolo 45 is prestellar in nature where a compact object is not formed yet, such as in the case of an

FHSC. Another candidate FHSC CB 17 MMS is observed to be consistent with that of starless cores and is ruled out to be an FHSC candidate (Spear et al. 2021).

As starless cores evolve toward collapse, the molecular deuterium fraction in the gas phase (e.g., $N_2D^+/N_2H^+$) increases and reaches a maximum at the onset of star formation (Crapsi et al. 2005; Emprechtinger et al. 2009; Tatematsu et al. 2021). Once the protostar is formed inside the core, the deuterium fraction declines (Gerner et al. 2015; Sakai et al. 2022) as the star heats up the surrounding medium and dissociates deuterated species. As a consequence, the center of the observed $N_2D^+$ peak could be shifted away from the protostar, whereas the dust continuum peak remains unaltered and represents the envelope emission around the central protostar. Therefore, the shift in $N_2D^+$ emission and dust continuum peak could provide a possible indication of the evolution of the dense core. In the case of G208Walma, the continuum peak is observed in the middle of the dense core (in Figure 4(c)) and the approximate size of the dense core on both sides of the continuum peak appears the same. The $N_2D^+$ peak, however, is shifted by $\sim 500 \pm 300$ au. We compare this separation and outflow lobe length with other young known FHSC candidates and young protostars in Figure 5(b). G208Walma appears to be more evolved than the most promising candidates FHSC L1451-mm (Maureira et al. 2020), MC35-mm (Fujishiro et al. 2020, Tokuda et al. 2020), and comparable with the young protostar/candidate FHSC B1b-S (Hirano & Liu 2014). It might also be younger than Cha-MM1 (Chen et al. 2012). We caution, however, that high uncertainties in the measured separation prevent drawing a specific evolutionary trend.

The estimated $T_{bol}$ and $L_{bol}$ for G208Walma (Appendix B) suggest that a protostar may have already formed inside the core, although it is not much evolved toward the Class 0 phase. In Figure 5(c), we compare the SED of G208Walma with other known candidate FHSCs and average early Class 0 spectra ($T_{bol} < 50$ K) from Enoch et al. (2009). From 24 $\mu$m and above, G208Walma spectra fairly resembles the candidate FHSCs with the SED peak around 150–250 $\mu$m.

## 5. Conclusions

In this work, we analyze ALMA observations at the 1.3 mm continuum and molecular line emission for the object G208Walma. The observations suggest a low-velocity outflow from G208Walma is present (observed velocity $\sim 4.2$ km s$^{-1}$ and corresponding deprojected $V_j \sim 24.0$ km s$^{-1}$), with compact SiO emission along the outflow suggesting the presence of a dense jet. We estimate a smaller jet mass-loss rate ($\dot{M}_j \sim 1.96 \times 10^{-7} M_\odot$ yr$^{-1}$) and smaller outflow force ($F_{CO} \sim 0.8 \times 10^{-8} M_\odot$ km s$^{-1}$ yr$^{-1}$) than that of other observed protostars in the literature. The dynamical time ($t_{dyn} \sim 930^{+200}_{-100}$ yr), extended 1.3 mm emission ($R_{eff} \sim 2500$ au), extended and offset $N_2D^+$ emission, and the SED suggest that
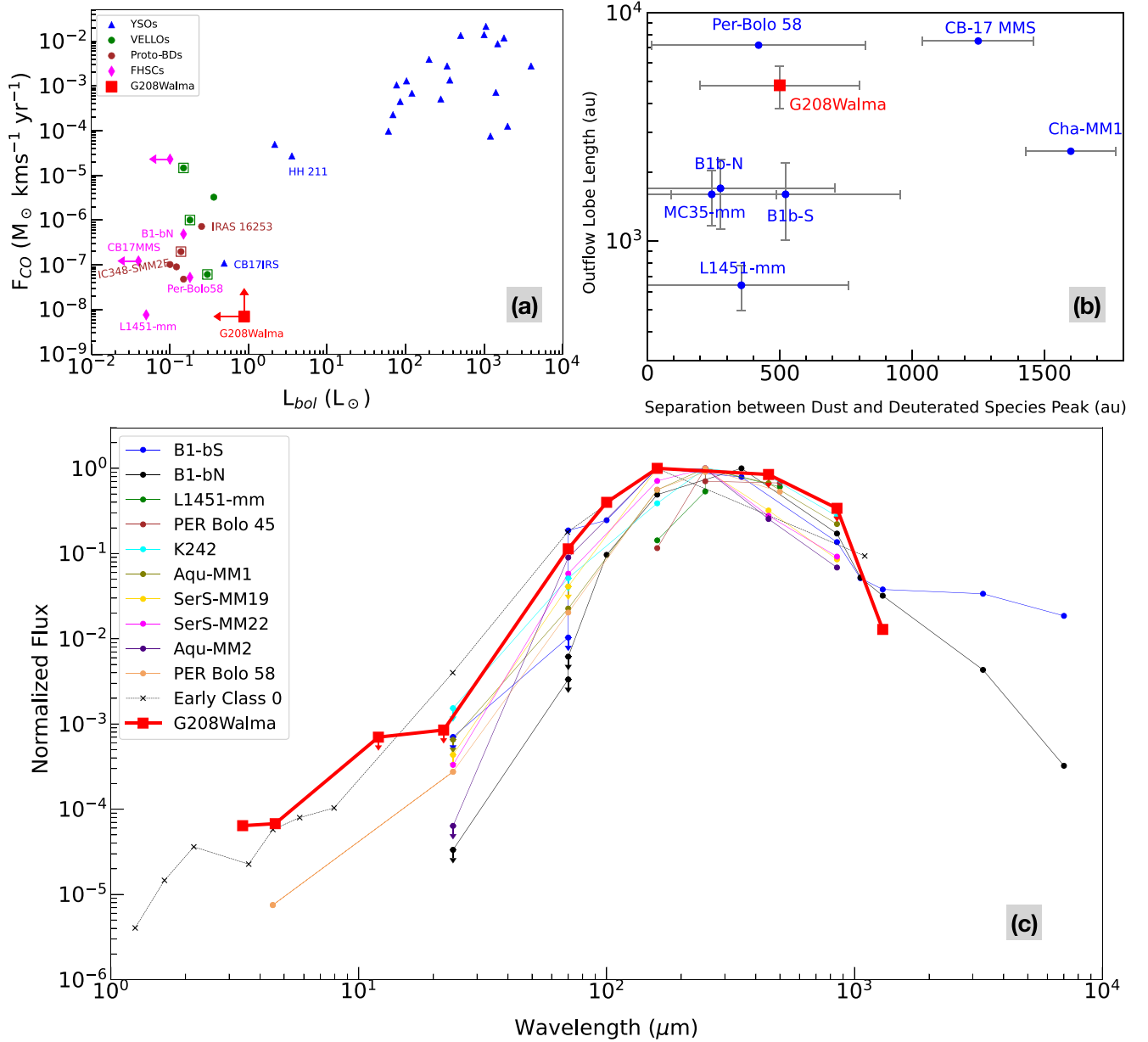
**Figure 5.** (a) $F_{CO}$ is plotted as a function of $L_{bol}$. The figure is reproduced following Figure 7 of Palau et al. (2014) and Figure 13 of Hsieh et al. (2016). The red rectangle represents the G208Walma. Blue, green, brown, and magenta points represent YSOs, VeLLOs, proto-BDs, and candidate FHSCs. Proto-BDs are also in the VeLLOs category. Open squares indicate single-dish observations. The arrows attached to $F_{CO}$ and $L_{bol}$ for G208Walma indicate lower and upper limits, respectively. (b) CO outflow lobe length vs. separation between dust continuum and deuterated species peaks for different candidate FHSCs and early protostars (marked with names). This figure is reproduced from Figure 14 (bottom panels) of Maureira et al. (2020), and G208Walma is added by the red rectangle. (c) Comparison of the normalized SED of G208Walma with literature candidate FHSCs and early protostars, following Figure 14 (top panel) of Maureira et al. (2020). The corresponding multiwavelength fluxes (Table B1) and references (Table B2) are presented in Appendix B. Different colors represent different objects and the average early Class 0 SED ($T_{bol} < 50$ K). G208Walma is shown as a red line with rectangular points.

the source is at the very early stage of protostellar evolution, possibly within a few hundred years of the second collapse. Therefore, G208Walma could be the earliest protostellar object with a molecular jet observed to date.

# Appendix A
## CO Emission and Jet/Outflow Parameters

### A.1. Channel Maps and Spectra

Figure A1 displays the CO channel maps at different velocities. The outflow emission channels in the southern lobe range from $V_{obs} = 2.8$ to $8.4\,km\,s^{-1}$. The channel at $V_{obs} \sim 8.4\,km\,s^{-1}$ is possibly showing both outflow and ambient material. The northern channels range from $V_{obs} = 4.2$ to $8.4\,km\,s^{-1}$, where the channel at $V_{obs} = 2.8\,km\,s^{-1}$ also shows some faint emission. The systemic velocity of G208Walma is $V_{sys} = 7.0\,km\,s^{-1}$. For both lobes, the maximum flow velocities are considered to be $V_{off} = |V_{obs} - V_{sys}| = 4.2\,km\,s^{-1}$. The outflow emission in the southern and northern velocity channels are not equally distributed on both sides of $V_{sys}$, therefore, it is difficult to define blueshifted and redshifted emission precisely for G208Walma. Such outflow velocity structure around $V_{sys}$ suggests a small inclination angle of the system. The channels from $V_{obs} = 7.0$–$11.2\,km\,s^{-1}$ indicate that the tip of the southern jet/outflow lobe is possibly colliding with ambient material. Thus, the SiO emission at the outermost part of the southern lobe could be a combination of jet emission and a collision zone.

Spectra in CO and SiO emission from a rectangular region along the outflow/jet axis are displayed in Figure A2. The SiO emission is confined between 2.8 and $10\,km\,s^{-1}$. The CO emission has two peaks: one at $V_{sys} \sim 7.0\,km\,s^{-1}$ and another at $\sim 12.0$–$14.0\,km\,s^{-1}$. From channel maps in Figure A1, it is obvious that there is no counterpart in the CO outflow at a velocity of $9.8\,km\,s^{-1}$ and above. The SiO spectra also confirmed that the second peak at $\sim 12.0$–$14.0\,km\,s^{-1}$ is not associated with G208Walma. In the spectra of CO and SiO, there is no clear differentiation between the high-velocity and low-velocity components. Therefore, it is difficult to distinguish between the low-velocity CO outflow (wind component) and the high-velocity jet component based on the velocity distribution only.
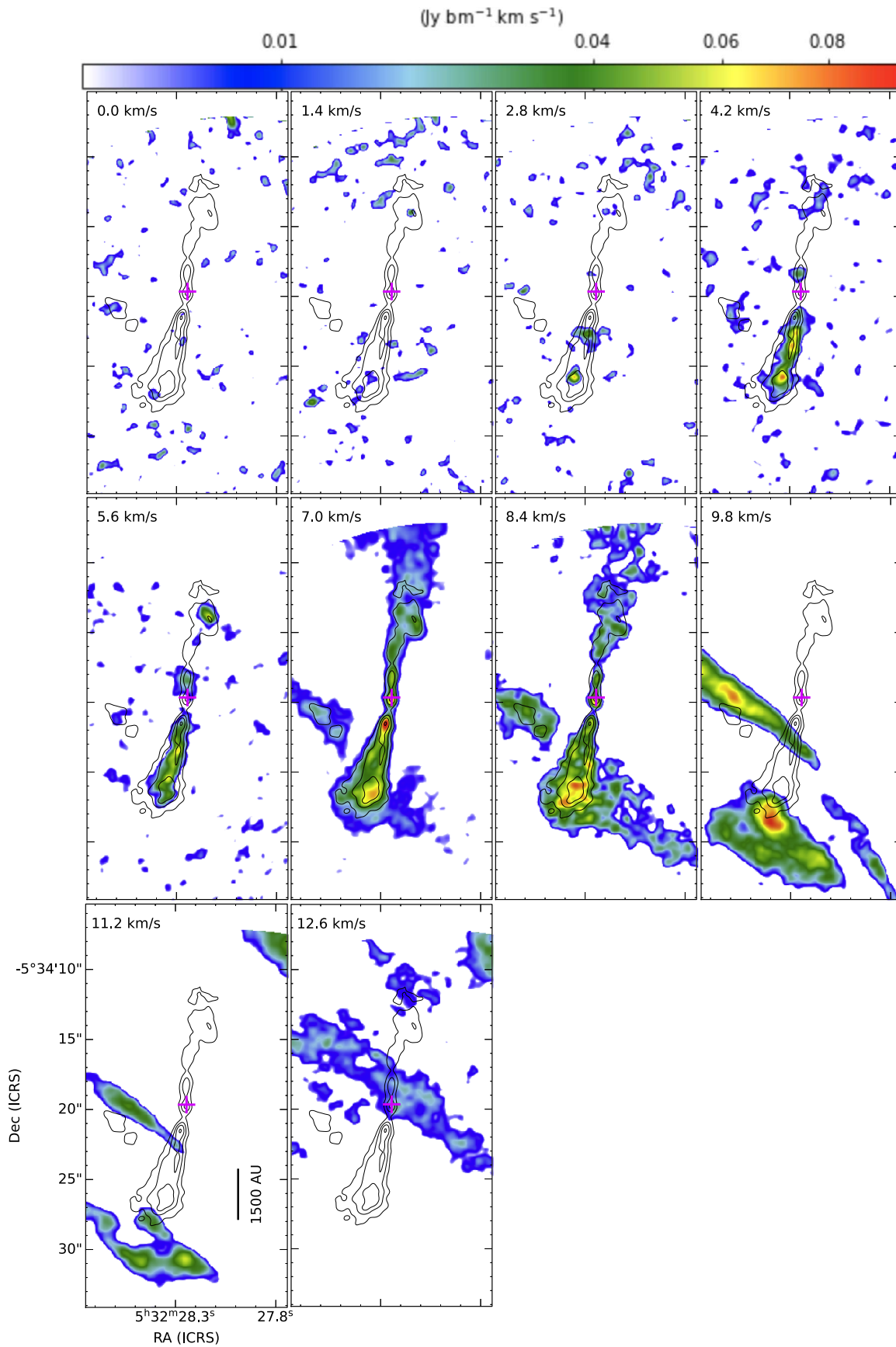
**Figure A1.** Channel maps of $^{12}$CO(2−1) emission in color scale. The black contours represent the integrated CO emission and have the same meaning as Figure 1(a). The corresponding channel velocities are mentioned in each panel. The magenta cross is the 1.3 mm continuum peak. A linear scale bar is shown in the lower-left panel (at channel $V_{\rm obs} = 11.2$ km s$^{-1}$).
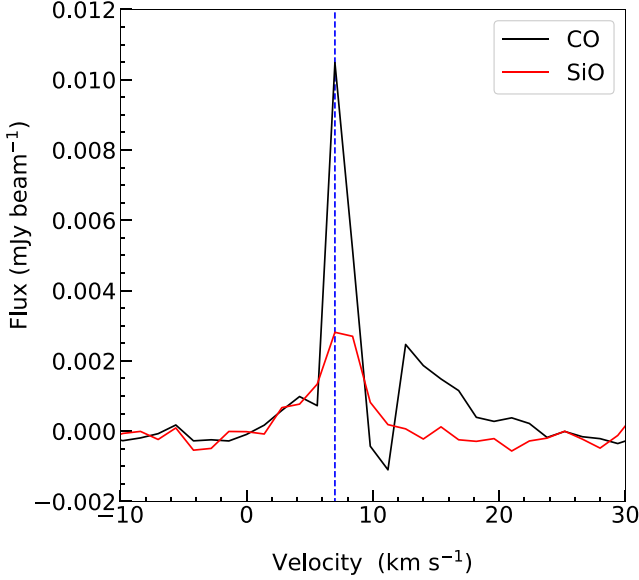
**Figure A2.** Spectra of CO (in black) and SiO (in red) emission extracted from a box region along an outflow/jet axis, which covers the total CO and SiO emission, respectively. The systemic velocity at $V_{\rm sys} = 7.0$ km s$^{-1}$ is marked by a vertical blue dashed line.

### A.2. Jet Mass-loss Rate

The jet mass-loss rate $\dot{M}_j$ was derived from the CO emission flux for a specific excitation temperature of $T_{\rm ex}$ within the jet. Under the assumption of optically thin CO emission, the beam-average CO column densities ($N_{\rm CO}$) were measured, which is then converted into beam-averaged H$_2$ column density $N_{\rm H_2}$ for CO abundance ratio, $X_{\rm CO} = N_{\rm CO}/N_{\rm H_2}$. We assume that the molecular jet is flowing through a uniform cylinder at a constant density and speed of gas along the transverse beam direction. Because the jet is not resolved at the present spatial resolution, the beam size ($b_m$) is taken to be the jet width. Thus, $\dot{M}_j$ can be expressed as

$$\dot{M}_j = \mu_{\rm H_2} m_H \frac{N_{\rm CO}}{X_{\rm CO}} V_j b_m, \tag{A1}$$

where $\mu_{H2} = 2.8$ is the mean molecular weight and $m_H$ is the mass of a hydrogen atom. $V_j$ is the mean deprojected jet velocity.

### A.3. Outflow Force

We derive the outflow force ($F_{\rm CO}$) from the CO emission. First, the outflow emission above $3\sigma$ in the $k$th channel is converted to outflow mass ($M_k$) for each velocity channel following the equation (Yıldız et al. 2015):

$$M_k = \mu_{\rm H_2} m_H A \frac{\sum_l N_{CO,l}}{X_{\rm CO}}, \tag{A2}$$

where the sum is over all outflow pixels $l$ on the $k$th channel. $N_{\rm CO}$ is the beam-average CO column density. $A$ is the surface area of each pixel, and the CO abundance ratio $X_{\rm CO} \sim 10^{-4}$ in the jet. In the next step, for the outflow extension of $R_{\rm CO}$ and maximum outflow velocity ($V_{\rm CO,max}$), $F_{\rm CO}$ can be expressed as (Yıldız et al. 2015)

$$F_{\rm CO} = f_{ia} \frac{V_{\rm CO,max} \sum_k M_k V_k}{R_{\rm CO}}, \tag{A3}$$

where the momentum ($P$) on the $k$th channel is $M_k V_k$ for a mass $M_k$ with the central velocity $V_k$ ($= |V_{\rm obs} - V_{\rm sys}|$). The factor $f_{ia}$ deals with the inclination correction.

### Appendix B
### Spectral Energy Distribution

We searched published catalogs for a compact continuum counterpart to G208Walma within a search radius of $3''$ from the 1.3 continuum peak (see Dutta et al. 2015 for more details on the catalog-matching method). The Wide-field Infrared Survey Explorer (WISE; Wright et al. 2010) and Herschel Space Observatory (https://sci.esa.int/web/herschel) data were obtained from the IRSA IPAC catalog (https://irsa.ipac.caltech.edu/). It matches with WISE catalog source J053228.14–053420.6. James Clerk Maxwell Telescope (JCMT) data were obtained from Mairs et al. (2016, island #25). The multiwavelength fluxes are listed in Table B1. Based on the poor signal-to-noise ratio, the fluxes at WISE 12 $\mu$m, 24 $\mu$m, and JCMT 450 $\mu$m, 850 $\mu$m are considered upper limit measurements. The references to the multiwavelength fluxes of Figure 5c are also listed in Table B2. $T_{\rm bol}$ and $L_{\rm bol}$ were derived using the trapezoid rule of integration over all the observed fluxes. Following Myers & Ladd (1993), the flux-weighted mean frequencies in the observed SED were used to estimate $T_{\rm bol}$. We obtained $T_{\rm bol} \sim 31$ K and $L_{\rm bol} \sim 0.8\,L_\odot$. Based on the uncertainty in the observed fluxes, we assume these values are at the upper limit.

**Table B1**
Multiwavelength Flux of G208Walma

| Wavelength ($\mu$m) | Flux (mJy) | Error (mJy) | Reference Telescope |
|---|---|---|---|
| 3.4 | 0.3435 | 0.0261 | WISE |
| 4.6 | 0.3626 | 0.0256 | WISE |
| 12.0 | 3.7558 | 1.2804 | WISE |
| 22.0 | 4.45537 | … | WISE |
| 70.0 | 609.079 | 13.356 | Herschel |
| 100.0 | 2139.573 | 58.847 | Herschel |
| 160.0 | 5359.623 | 17.7 | Herschel |
| 450.0 | 4540.0 | … | JCMT |
| 850.0 | 1820.0 | … | JCMT |
| 1300.0 | 69.0 | 3.5 | ALMA; This study |

**Table B2**
References for Multiwavelength Fluxes of Figure 5(c)

| Sources | Catalog reference |
|---|---|
| B1-bN | Hirano & Liu (2014) |
| B1-bS | Hirano & Liu (2014) |
| L1451-mm | Maureira et al. (2020) |
| PER Bolo 45 | Maureira et al. (2020) |
| K242 | Young et al. (2018) |
| Aqu-MM1 | Young et al. (2018) |
| SerpS-MM19 | Young et al. (2018) |
| SerpS-MM22 | Young et al. (2018) |
| Aqu-MM2 | Young et al. (2018) |
| PER Bolo 58 | Enoch et al. (2010), Maureira et al. (2020) |
| Average Early Class 0 | Enoch et al. (2009) |

## ORCID iDs

Somnath Dutta ● https://orcid.org/0000-0002-2338-4583
Chin-Fei Lee ● https://orcid.org/0000-0002-3024-5864
Naomi Hirano ● https://orcid.org/0000-0001-9304-7884
Tie Liu ● https://orcid.org/0000-0002-5286-2564
Doug Johnstone ● https://orcid.org/0000-0002-6773-459X
Sheng-Yuan Liu ● https://orcid.org/0000-0003-4603-7119
Ken'ichi Tatematsu ● https://orcid.org/0000-0002-8149-8546
Paul F. Goldsmith ● https://orcid.org/0000-0002-6622-8396
Dipen Sahu ● https://orcid.org/0000-0002-4393-3463
Neal J. Evans ● https://orcid.org/0000-0001-5175-1777
Patricio Sanhueza ● https://orcid.org/0000-0002-7125-7685
Woojin Kwon ● https://orcid.org/0000-0003-4022-4132
Sheng-Li Qin ● https://orcid.org/0000-0003-2302-0613
Manash Ranjan Samal ● https://orcid.org/0000-0002-9431-6297
Qizhou Zhang ● https://orcid.org/0000-0003-2384-6589
Kee-Tae Kim ● https://orcid.org/0000-0003-2412-7092
Hsien Shang ● https://orcid.org/0000-0001-8385-9838
Chang Won Lee ● https://orcid.org/0000-0002-3179-6334
Kai-Syun Jhan ● https://orcid.org/0000-0003-2069-1403
Shanghuo Li ● https://orcid.org/0000-0003-1275-5251
Jeong-Eun Lee ● https://orcid.org/0000-0003-3119-2087
Alessio Traficante ● https://orcid.org/0000-0003-1665-6402
Mika Juvela ● https://orcid.org/0000-0002-5809-4834
Leonardo Bronfman ● https://orcid.org/0000-0002-9574-8454
David Eden ● https://orcid.org/0000-0002-5881-3229
Archana Soam ● https://orcid.org/0000-0002-6386-2906
Jinhua He ● https://orcid.org/0000-0002-3938-4393
Hong-li Liu ● https://orcid.org/0000-0003-3343-9645
Yi-Jehng Kuan ● https://orcid.org/0000-0002-4336-0730
Veli-Matti Pelkonen ● https://orcid.org/0000-0002-8898-1047
Hee-Weon Yi ● https://orcid.org/0000-0003-0537-5461
Shih-Ying Hsu ● https://orcid.org/0000-0002-1369-1563

## References

Allen, A., Li, Z.-Y., & Shu, F. H. 2003, ApJ, 599, 363
Astropy Collaboration, Robitaille, T. P., Tollerud, E. L., et al. 2013, A&A, 558, A33
Balança, C., Dayou, F., Faure, A., Wiesenfeld, L., & Feautrier, N. 2018, MNRAS, 479, 2692
Bally, J. 2016, ARA&A, 54, 491
Bjerkeli, P., Ramsey, J. P., Harsono, D., et al. 2019, A&A, 631, A64
Bontemps, S., Andre, P., Terebey, S., & Cabrit, S. 1996, A&A, 311, 858
Chen, X., Arce, H. G., Dunham, M. M., et al. 2012, ApJ, 751, 89
Ciardi, A., & Hennebelle, P. 2010, MNRAS, 409, L39
Crapsi, A., Caselli, P., Walmsley, C. M., et al. 2005, ApJ, 619, 379
Dutta, S., Mondal, S., Jose, J., et al. 2015, MNRAS, 454, 3597
Dutta, S., Lee, C.-F., Liu, T., et al. 2020, ApJS, 251, 20
Dutta, S., Lee, C.-F., Johnstone, D., et al. 2022, ApJ, 925, 11
Emprechtinger, M., Caselli, P., Volgenau, N. H., Stutzki, J., & Wiedner, M. C. 2009, A&A, 493, 89
Enoch, M. L., Evans, N. J. I., Sargent, A. I., & Glenn, J. 2009, ApJ, 692, 973
Enoch, M. L., Lee, J.-E., Harvey, P., Dunham, M. M., & Schnee, S. 2010, ApJL, 722, L33
Fujishiro, K., Tokuda, K., Tachihara, K., et al. 2020, ApJL, 899, L10
Galli, D., & Shu, F. H. 1993, ApJ, 417, 220
Gerner, T., Shirley, Y. L., Beuther, H., et al. 2015, A&A, 579, A80
Gibb, A. G., Richer, J. S., Chandler, C. J., & Davis, C. J. 2004, ApJ, 603, 198
Glassgold, A. E., Mamon, G. A., & Huggins, P. J. 1991, ApJ, 373, 254
Hennebelle, P., & Fromang, S. 2008, A&A, 477, 9
Hirano, N., Ho, P. P. T., Liu, S.-Y., et al. 2010, ApJ, 717, 58
Hirano, N., & Liu, F.-c 2014, ApJ, 789, 50
Hsieh, T.-H., Lai, S.-P., Belloche, A., & Wyrowski, F. 2016, ApJ, 826, 68
Hunter, J. D. 2007, CSE, 9, 90
Kounkel, M., Covey, K., Suárez, G., et al. 2018, AJ, 156, 84
Larson, R. B. 1969, MNRAS, 145, 271
Lee, C.-F. 2020, A&ARv, 28, 1
Lee, C.-F., Hasegawa, T. I., Hirano, N., et al. 2010, ApJ, 713, 731
Lee, C.-F., Ho, P. T. P., Hirano, N., et al. 2007, ApJ, 659, 499
Lee, C.-F., Li, Z.-Y., Hirano, N., et al. 2018, ApJ, 863, 94
Lee, C.-F., Mundy, L. G., Reipurth, B., Ostriker, E. C., & Stone, J. M. 2000, ApJ, 542, 925
Li, Z.-Y., & Shu, F. H. 1996, ApJ, 472, 211
Lizano, S., & Shu, F. H. 1987, in ASI Conf. Ser. 210, Physical Processes in Interstellar Clouds, ed. G. E. Morfill & M. Scholer (Dordrecht: Reidel), 173
Machida, M. N. 2014, ApJL, 796, L17
Machida, M. N., & Basu, S. 2019, ApJ, 876, 149
Mairs, S., Johnstone, D., Kirk, H., et al. 2016, MNRAS, 461, 4022
Maureira, M. J., Arce, H. G., Dunham, M. M., et al. 2020, MNRAS, 499, 4394
McMullin, J. P., Waters, B., Schiebel, D., Young, W., & Golap, K. 2007, in ASP Conf. Ser. 376, CASA Architecture and Applications, ed. R. A. Shaw, F. Hill, & D. J. Bell (San Francisco, CA: ASP), 127
Mellon, R. R., & Li, Z.-Y. 2008, ApJ, 681, 1356
Millan-Gabet, R., Malbet, F., Akeson, R., et al. 2007, in Protostars and Planets V, ed. B. Reipurth, D. Jewitt, & K. Keil (Tucson, AZ: Univ. Arizona Press), 539
Müller, H. S. P., Thorwirth, S., Roth, D. A., & Winnewisser, G. 2001, A&A, 370, L49
Myers, P. C., & Ladd, E. F. 1993, ApJL, 413, L47
Nakano, T. 1979, PASJ, 31, 697
Öberg, K. I., Guzmán, V. V., Merchantz, C. J., et al. 2017, ApJ, 839, 43
Ossenkopf, V., & Henning, T. 1994, A&A, 291, 943
Palau, A., Zapata, L. A., Rodríguez, L. F., et al. 2014, MNRAS, 444, 833
Podio, L., Tabone, B., Codella, C., et al. 2021, A&A, 648, A45
Robitaille, T., & Bressert, E. 2012, APLpy: Astronomical Plotting Library in Python, Astrophysics Source Code Library, ascl:1208.017
Sakai, T., Sanhueza, P., Furuya, K., et al. 2022, ApJ, 925, 144
Schilke, P., Walmsley, C. M., Pineau des Forets, G., & Flower, D. R. 1997, A&A, 321, 293
Schnee, S., Di Francesco, J., Enoch, M., et al. 2012, ApJ, 745, 18
Shu, F. H. 1977, ApJ, 214, 488

Shu, F. H., Adams, F. C., & Lizano, S. 1987, ARA&A, 25, 23
Spear, S., José Maureira, M., Arce, H. G., et al. 2021, ApJ, 923, 231
Tabone, B., Godard, B., Pineau des Forêts, G., Cabrit, S., & van Dishoeck, E. F. 2020, A&A, 636, A60
Tatematsu, K., Kim, G., Liu, T., et al. 2021, ApJS, 256, 25
Tokuda, K., Fujishiro, K., Tachihara, K., et al. 2020, ApJ, 899, 10

Tomisaka, K. 2002, ApJ, 575, 306
Wright, E. L., Eisenhardt, P. R. M., Mainzer, A. K., et al. 2010, AJ, 140, 1868
Yıldız, U. A., Kristensen, L. E., van Dishoeck, E. F., et al. 2015, A&A, 576, A109
Young, A. K., Bate, M. R., Mowat, C. F., Hatchell, J., & Harries, T. J. 2018, MNRAS, 474, 800